ROYAL SOCIETY OF CHEMISTRY

PAPER

Selective conversion of CO_2 to CH_4 enhanced by WO_3/In_2O_3 S-scheme heterojunction photocatalysts with efficient CO_2 activation†

Ying He,[a] Zhengpeng Yang,[a] Jiaguo Yu,[a] Difa Xu,[b] Chengyuan Liu,[c] Yang Pan,[c] Wojciech Macyk[d] and Feiyan Xu ✱[a]

Solar-powered CO_2 reduction is a promising approach for mitigating the energy crisis and environmental issues. However, its efficiency is hindered by challenges including difficult CO_2 activation, rapid charge recombination, and uncontrollable selectivity. Here, we develop WO_3/In_2O_3 S-scheme heterojunction photocatalysts by depositing In_2O_3 nanoparticles onto WO_3 nanosheets for CO_2 photoreduction. The Fermi level difference triggers electron transfer upon coupling, generating an internal electric field pointing from In_2O_3 to WO_3 at the interface. This impels oriented charge transfer and effective separation of the powerful photoinduced carriers. With the unique S-scheme mechanism and the efficient activation of CO_2 molecules on the In_2O_3 surface, the resulting WO_3/In_2O_3 heterostructures exhibit enhanced CO_2 photoreduction performance with ~53.7% selectivity for CH_4, without any molecule cocatalyst or scavenger. *In situ* irradiation X-ray photoelectron spectroscopy, *in situ* diffuse reflectance infrared Fourier transform spectroscopy, along with density functional theory simulations are conducted to elucidate the photocatalytic and CO_2-reduction mechanism, and the enhanced CH_4-selectivity.

1. Introduction

Recently, the incessant combustion of fossil fuels has led to a substantial increase in atmospheric carbon dioxide (CO_2) concentration, causing grave environmental pollution and concerns about energy scarcity.[1–9] To tackle these issues, a promising strategy is the photocatalytic reduction of CO_2 to valuable solar fuels driven by abundant, clean, and inexhaustible sunlight.[10,11] Nevertheless, the linear CO_2 molecules exhibit thermodynamic stability with a high dissociation energy of the C=O bond (~750 kJ mol^{-1}), making their adsorption and activation onto the catalyst surface challenging.[12,13] Additionally, the CO_2 photoreduction process is intricate and involves multiple photoelectron transfer, which leads to diverse reduction products, including CO, CH_4, CH_3OH, *etc.*, with unpredictable selectivity. Although CH_4, the major component of

natural gas, has the lowest reduction potential among all the products (−0.24 V *vs.* NHE), it requires eight photoelectrons, making it more difficult to produce than others from a kinetic perspective. Although a variety of photocatalysts have been reported for CO_2 reduction to CH_4,[14–21] most still suffer from uncontrollable selectivity and low conversion efficiency. Thus, designing highly active photocatalysts with efficient CO_2 activation and high CH_4 selectivity is still a daunting task.

Indium oxide (In_2O_3) is a popular reduction photocatalyst with a high conduction band level, narrow band gap (~2.8 eV) and visible light absorption.[22,23] It has been reported that stable CO_2 molecules can be highly activated on the In_2O_3 surface to enhance CO_2 photoreduction activity, but the selectivity of CH_4 has not been modulated.[22] In addition, the recombination of photogenerated carriers in unitary In_2O_3 occurs more readily than transferring to the catalyst surface to participate in photoreactions, leading to poor photocatalytic performance.[24,25] Therefore, the development of In_2O_3-based heterojunction photocatalysts that enable efficient spatial separation of electron/hole pairs and selective CO_2-to-CH_4 conversion enhancement is desirable but challenging.

Coupling two semiconductors to fabricate an S-scheme heterojunction offers tremendous potential in augmenting photo-activity, owing to the effective separation of photogenerated carriers and their robust redox capability.[8,26–28] Generally, S-scheme heterojunctions are constituted of oxidation and reduction photocatalysts. The variance in their Fermi levels

[a]*Laboratory of Solar Fuel, Faculty of Materials Science and Chemistry, China University of Geosciences, 68 Jincheng Street, Wuhan 430078, P. R. China. E-mail: xufeiyan@cug.edu.cn*

[b]*Hunan Key Laboratory of Applied Environmental Photocatalysis, Changsha University, Changsha, 410022, P. R. China*

[c]*National Synchrotron Radiation Laboratory, University of Science and Technology of China, Hefei, 230026, P. R. China*

[d]*Faculty of Chemistry, Jagiellonian University, ul. Gronostajowa 2, Kraków 30-387, Poland*

elicits electron transfer upon contact, thereby resulting in the bending of energy bands and the creation of an internal electric field (IEF) at their interface. As a consequence of the bent bands, IEF, and coulombic attraction, the futile photogenerated electrons in the oxidation photocatalyst and the holes in the reduction photocatalyst amalgamate, accomplishing the efficient spatial separation of charge carriers with adequate redox ability to boost the photocatalytic performance.[29–32] Tungsten trioxide (WO_3) is an oxidation photocatalyst that exhibits visible-light response and potent oxidizing ability, attributable to its narrow band gap (2.4–2.8 eV) and positive valence band position.[33,34] Given the interweaved band structures and disparity in work functions, the combination of In_2O_3 with WO_3 might engender a desirable S-scheme heterojunction photocatalyst with anticipated charge separation, strong redox ability, and heightened CO_2 activation, thereby enhancing CO_2 photoreduction performance.[22,35,36]

Herein, we synthesized WO_3/In_2O_3 S-scheme heterojunction photocatalysts by depositing In_2O_3 nanoparticles on WO_3 nanosheets through an immersion-annealing technique. Compared to pure WO_3, the resulting WO_3/In_2O_3 heterostructures revealed elevated selectivity in the conversion of CO_2 into CH_4 (53.7%) and enhanced CO_2 reduction efficiency without any molecular cocatalyst or scavenger. Such superior performance was ascribed to the S-scheme charge transfer mechanism and the effective CO_2 activation on the In_2O_3 surface, which were verified through *in situ* irradiation X-ray photoelectron spectroscopy (XPS), time-resolved photoluminescence spectroscopy (TRPL), density functional theory (DFT) calculation and temperature-programmed desorption of CO_2 (CO_2-TPD). *In situ* diffuse reflectance infrared Fourier transform spectroscopy (DRIFTS) and theoretical simulations were also employed to elucidate the CO_2 reduction mechanism and the potential causes for the high selectivity of CH_4. Our work may present a novel perspective for designing exceptional S-scheme heterojunction photocatalysts that facilitate efficient CO_2 activation and improved selective CO_2-to-CH_4 conversion.

2. Experimental details

2.1 Synthesis of $WO_3 \cdot H_2O$ nanosheets

Typically, a total of 3.6 mmol of sodium tungstate dihydrate ($Na_2WO_4 \cdot 2H_2O$) and 3.0 mL of tetrafluoroboric acid (HBF_4, 40 wt%) were dissolved in 60 mL of deionized water. The resulting light-yellow solution was transferred to a 100 mL Teflon-lined stainless autoclave and reacted at 100 °C for 12 h. Upon completion of the reaction, yellow precipitates were centrifuged and washed with deionized water and ethanol for three times, followed by drying at 80 °C in an oven to obtain the $WO_3 \cdot H_2O$ nanosheets.

2.2 Preparation of WO_3/In_2O_3 heterostructures

A certain amount of indium nitrate ($In(NO_3)_3 \cdot 4H_2O$) was added to a 30 mL aqueous solution containing 200 mg of $WO_3 \cdot H_2O$ nanosheets. The mixture was magnetically stirred for 2 h, followed by drying in an oven at 90 °C. The resulting solid products

were annealed in air at 500 °C for 2 h, with a heating rate of 2 °C min^{-1}. The obtained WO_3/In_2O_3 heterostructures were labelled as WIx ($x = 5, 10$ and 15), where W and I represent WO_3 and In_2O_3 respectively; x is the molar ratio of In_2O_3 in WO_3/In_2O_3 nanohybrids.

3. Results and discussion

3.1 Activation and photoreduction of CO_2 over WO_3/In_2O_3 heterojunctions

The adsorption and activation of CO_2 molecules on catalysts were first investigated by DFT calculations since they are essential steps for CO_2 photoreduction. Fig. 1a and b show that when CO_2 is adsorbed onto the In_2O_3 surface, the O=C=O bond is visibly bent at an angle of 129.33°, and the bond length is stretched in comparison with free CO_2 molecules (1.16 Å). Both the C and O atoms of CO_2 form chemical bonds with the O and In atoms of In_2O_3. Moreover, In_2O_3 donates 0.2 electrons to CO_2 when CO_2 adsorbs on In_2O_3 (Fig. 1c), which is further supported by the planar-averaged charge density difference along the Z direction as shown in Fig. S1.† The investigation of the CO_2 adsorption capability reveals that pure In_2O_3 and WI10 exhibit stronger CO_2 adsorption compared to pristine WO_3, following the same trend as the N_2 adsorption (Fig. S2 and Table S1†). The CO_2-TPD results demonstrate that pure WO_3, In_2O_3 and WI10 all display desorption peaks at 80–200 °C assigned to the physical adsorption of CO_2 (Fig. 1d).[37–39] In the temperature range of 400–800 °C, no significant signals are detected over pristine WO_3. However, both pure In_2O_3 and WI10 reveal three prominent desorption peaks corresponding to the decomposition of b-CO_3^{2-} (~450 °C) and m-CO_3^{2-} (550–750 °C) species, suggesting strong chemisorption interactions between CO_2 molecules and In_2O_3.[40–42] Furthermore, *in situ* DRIFTS spectra obtained after adsorption of CO_2 for 15, 30, 45, and 60 min exhibit distinct peaks of formaldehyde (HCHO) (1750 and 1770 cm^{-1}), monodentate carbonate (m-CO_3^{2-}) (1590, 1560 and 1540 cm^{-1}), bidentate carbonate (b-CO_3^{2-}) (1425, 1410, 1380, and 1340 cm^{-1}), and bicarbonate (HCO_3^-) (1180, 1110 and 1030 cm^{-1}) over In_2O_3 and WI10 (Fig. S3†). These results indicate that CO_2 can be chemisorbed and activated by In_2O_3, and In_2O_3 is the preferable active site for CO_2 photoreduction in the heterojunctions.

The photocatalytic performance toward CO_2 reduction was evaluated in an online closed gas-circulation system (OLPCRS-2, Shanghai Boyi Scientific Instrument Co., Ltd) with a quartz reactor under visible light irradiation (Fig. S4†). CO and CH_4 were identified as the reduction products, and O_2 was determined as the oxidation product. Control experiments revealed that no product can be detected in the dark or in the absence of CO_2. As shown in Fig. 1e and f, pristine WO_3 and In_2O_3 both reveal lower production yields of CO and CH_4 due to the rapid recombination of photogenerated charge carriers within the unitary photocatalyst. After coupling WO_3 with In_2O_3, the CO_2 reduction efficiency is enhanced, reaching the highest evolution yield of 6.6 and 5.4 µmol g^{-1} for CO and CH_4 over WI10. Excessive loading of In_2O_3 nanoparticles on WO_3 nanosheets, *i.e.*, WI15, deteriorates the photocatalytic performance owing to

This journal is © The Royal Society of Chemistry 2023

J. Mater. Chem. A, 2023, **11**, 14860–14869 | **14861**

Fig. 1 (a and b) Optimized structure and (c) the corresponding charge density difference images of the CO_2 molecule adsorbed on the In_2O_3 (111) surface. (d) CO_2-TPD spectra of In_2O_3, WI10 and WO_3. Photocatalytic CO_2 reduction activities over WO_3, WIx, and In_2O_3 during the 12 h experiment performed under visible light irradiation: time course of (e) CO and (f) CH_4 production yields. (g) SVUV-PIMS spectra of the products collected after $^{13}CO_2$ photoreduction for WI10 at $h\nu$ = 14.2 eV. (h) The selectivity of CO and CH_4 over WO_3, WIx, and In_2O_3 samples.

14862 | J. Mater. Chem. A, 2023, 11, 14860–14869

This journal is © The Royal Society of Chemistry 2023

the light shielding effect. During CO_2 photoreduction, the photogenerated holes oxidize H_2O to produce O_2 in the absence of sacrificial agents, and the evolution rate of O_2 (Fig. S5†) follows the same tendency as that of CO and CH_4. The apparent quantum efficiency (AQE) of CO_2 photoreduction was measured at different monochromatic wavelengths including 365, 380, 400, 420, 450, and 500 nm over WO_3/In_2O_3 nanohybrids. Clearly, the trend of AQE matches well with the light absorption spectrum of WI10 (Table S2, Fig. S6†), affirming the photocatalytic nature of CO_2 reduction.[43–45] The synchrotron-radiation vacuum ultraviolet photoionization mass spectrometry (SVUV-PIMS) was employed to disclose the origin of the products by using isotope-labeled carbon dioxide ($^{13}CO_2$) as the substitute source gas. At a photon energy of 14.2 eV, the WO_3/In_2O_3 heterojunctions yield a mixture of $^{13}CH_4$ ($m/z = 17$) and ^{13}CO ($m/z = 29$) as shown in Fig. 1g, which confirms that the evolved reduction products indeed originate from the photoreduction of CO_2 rather than any carbonaceous impurities.[46]

Notably, the selectivity of CH_4 over WO_3/In_2O_3 nanohybrids is higher than that of CO and reaches the maximum of 53.7% over WI10 as revealed in Fig. 1h. In order to uncover the underlying reasons for the high selectivity of CH_4, as well as the reaction mechanism, *in situ* DRIFTS experiments along with DFT calculations were carried out. As shown in Fig. 2a, when CO_2/H_2O is introduced into the system in the dark, peaks of HCHO, $m\text{-}CO_3^{2-}$, $b\text{-}CO_3^{2-}$ and HCO_3^- are detected, strongly

remanifesting the chemisorption of CO_2 on the catalyst surface.[47,48] Under light irradiation, new adsorption peaks assigned to *COOH (1669 cm^{-1}), *CO (2079 cm^{-1}), *CHO (1012 cm^{-1}), *CH_2O (2855 cm^{-1}) and *CH_3O (1042 and 1181 cm^{-1}) are observed, which are significant intermediates in the conversion of CO_2 to CH_4.[49–51] Accordingly, a probable CO_2 photoreduction mechanism over WO_3/In_2O_3 composites is proposed as follows, where * stands for the active sites on WO_3/In_2O_3 heterojunctions.

$$* + CO_2 \rightarrow {}^*CO_2 \tag{1}$$

$$^*CO_2 + H^+ + e^- \rightarrow {}^*COOH \tag{2}$$

$$^*COOH + H^+ + e^- \rightarrow {}^*CO \tag{3}$$

$$^*CO + H^+ + e^- \rightarrow {}^*CHO \text{ or } {}^*CO \rightarrow CO + {}^* \tag{4}$$

$$^*CHO + H^+ + e^- \rightarrow {}^*CH_2O \tag{5}$$

$$^*CH_2O + H^+ + e^- \rightarrow {}^*CH_3O \tag{6}$$

$$^*CH_3O + H^+ + e^- \rightarrow CH_4 + {}^*O \tag{7}$$

$$^*O + H^+ + e^- \rightarrow {}^*OH \tag{8}$$

$$^*OH + H^+ + e^- \rightarrow {}^* + H_2O \tag{9}$$

Fig. 2 (a) *In situ* DRIFT spectra of WI10 after adsorption of CO_2/H_2O for 15, 30, 45, and 60 min in the dark, and then under light irradiation for 75, 90, 105, and 120 min. (b) Gibbs free energy diagram of CO_2 photoreduction over the In_2O_3 (111) slab.

This journal is © The Royal Society of Chemistry 2023

J. Mater. Chem. A, 2023, **11**, 14860–14869 | **14863**

Gibbs free energy (ΔG) calculation of CO_2 photoreduction over the In_2O_3 surface was further conducted to confirm the reaction pathway described above, and the results are presented in Fig. 2b. It is worth noting that the change in ΔG for the protonation of *CO to *CHO (pathway II, -1.61 eV) is much smaller than that for CO desorption form the catalyst surface (pathway I, -0.28 eV), providing a reasonable explanation for the high selectivity of CH_4 during CO_2 photoreduction.[52] Overall, the strong adsorption and activation of CO_2 molecules on the In_2O_3 surface are critical factors contributing to the enhanced CH_4 selectivity and CO_2 reduction performance.

3.2 Characterization of WO_3/In_2O_3 heterojunctions

Structural characterization studies provide additional insights into understanding the boosted photocatalytic activity. The X-ray diffraction (XRD) pattern of pure WO_3 is consistent with the standard monoclinic phase (JCPDS No. 20-1324), and pristine In_2O_3 is indexed to the cubic phase (JCPDS No. 71-2195), respectively (Fig. S7†). In the WI*x* nanohybrids, the intensity of diffraction peaks attributed to In_2O_3 increases with its content (*x*), indicating the synthesis of WO_3/In_2O_3 heterojunctions. The precursor $WO_3 \cdot H_2O$ exhibits uniform square nanosheets with a smooth surface as revealed in the field emission scanning electron microscopy (FESEM) image (Fig. S8†). After dehydration, pristine WO_3 maintains its nanosheet microscopy with some tiny surface wrinkles (Fig. 3a).[53] In FESEM and transmission electron microscopy (TEM) images of WO_3/In_2O_3 nanohybrids (WI10) (Fig. 3b and c), In_2O_3 nanoparticles are clearly observed to be deposited on the surface of WO_3 nanosheets. The high-resolution TEM image of WI10 (Fig. 3d) reveals distinct lattice fringes with spacings of 0.292 and 0.375 nm,
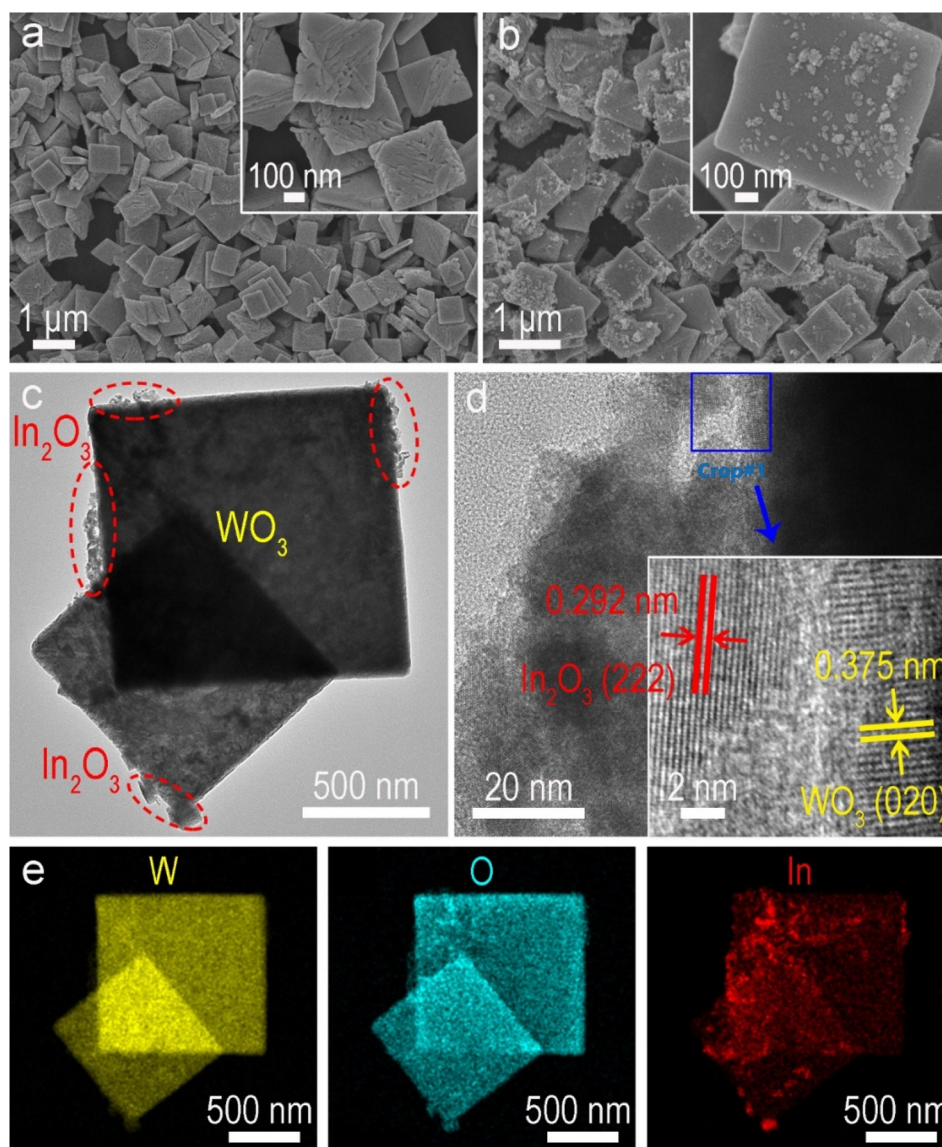

Fig. 3 (a) FESEM image of pure WO_3 nanosheets. (b) FESEM, (c) TEM and (d) HRTEM images of WO_3/In_2O_3 nanostructures (WI10). (e) EDX elemental mappings of W, O, and In elements in WO_3/In_2O_3 nanohybrids.

14864 | *J. Mater. Chem. A*, 2023, **11**, 14860–14869

This journal is © The Royal Society of Chemistry 2023

corresponding to In_2O_3 (222) and WO_3 (020) planes, respectively. The energy-dispersive X-ray spectroscopy (EDX) elemental mappings of WI10 confirm the existence of W, O and In elements, further affirming the formation of WO_3/In_2O_3 nanohybrids. The phase and morphology of spent WI10 were also evaluated, and there are no detectable changes compared with the fresh sample, indicating substantial photostability of the catalysts (Fig. S9†).

UV-vis diffuse reflectance spectroscopy (DRS) was employed to investigate the optical absorption properties of WO_3, In_2O_3 and WI10. The absorption edges of pure WO_3 and In_2O_3 are located at 470 and 465 nm, respectively, corresponding to the bandgap energies of 2.81 and 2.97 eV (Fig. S10†). The light harvesting of WI10 is slightly improved compared to pristine WO_3, indicating the successful hybridization of WO_3 and In_2O_3. XPS was carried out to analyze the chemical states and surface
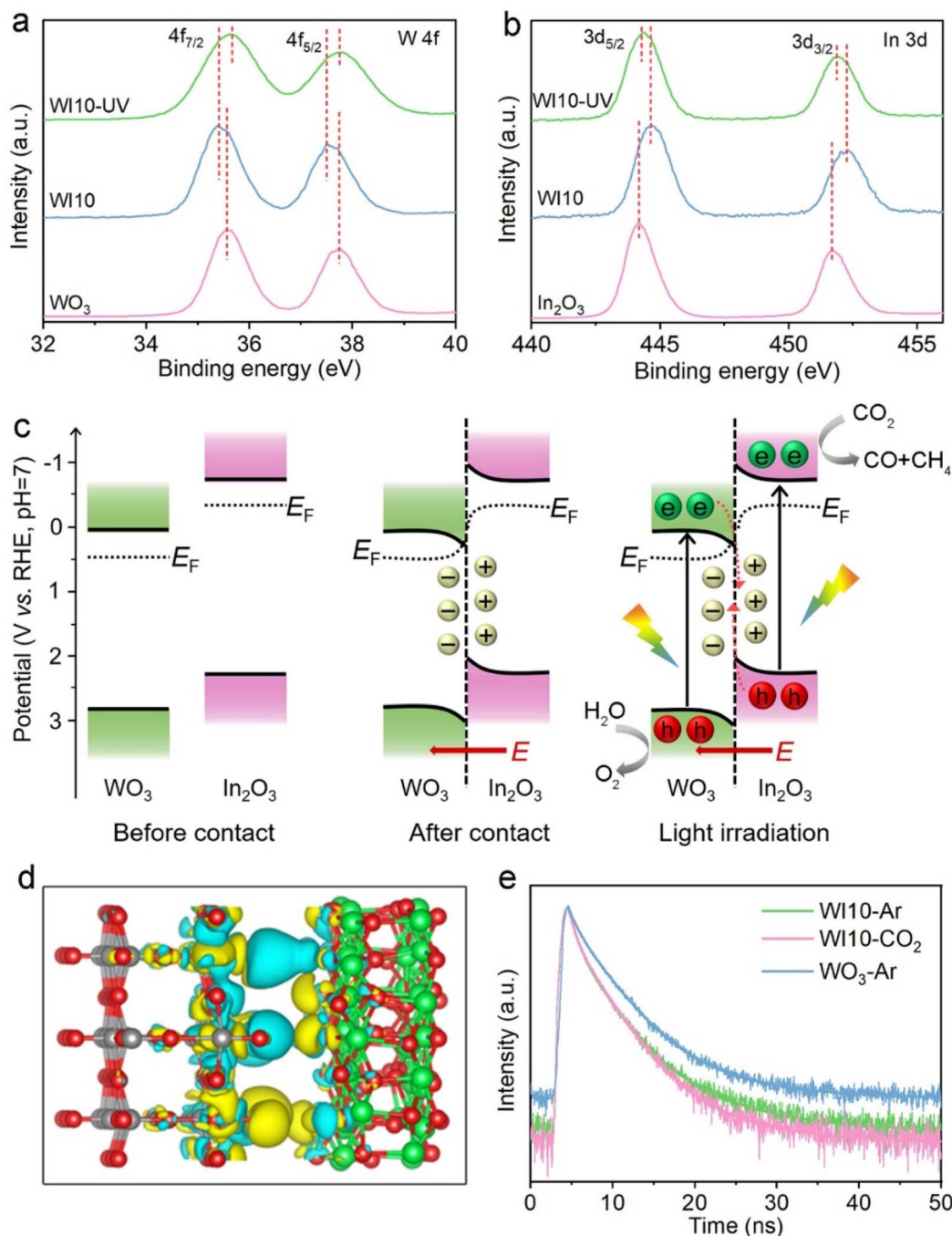

Fig. 4   High-resolution XPS spectra of (a) W 4f, (b) In 3d of WO_3, In_2O_3, and WI10. *In situ* irradiation XPS measurement was conducted under UV light irradiation. (c) Schematic illustration of the formation and charge separation of the WO_3/In_2O_3 S-scheme heterojunction. (d) The charge density difference of the WO_3/In_2O_3 heterojunctions; cyan and yellow regions represent electron depletion and accumulation, respectively; grey, green, and red spheres represent W, In and O atoms, respectively. (e) TRPL spectra of WO_3 and WI10 in different atmospheres.

compositions of the resultant samples. The survey spectrum of WI10 demonstrates the presence of the In element, as well as W and O elements derived from the WO_3 matrix (Fig. S11a†). The W 4f XPS spectra (Fig. 4a) exhibit two distinct peaks at 35.6 and 37.7 eV, corresponding to hexavalent W^{6+}.[54,55] The binding energies (BEs) of In $3d_{5/2}$ and In $3d_{3/2}$ are observed to be 444.2 and 451.7 eV, respectively, confirming the existence of trivalent In^{3+} (Fig. 4b).[56,57] After the photoreaction, the chemical states of WO_3/In_2O_3 heterojunctions exhibit imperceptible changes as manifested by the W 4f and In 3d XPS spectra (Fig. S12†), further confirming the stability of catalysts. The O 1s XPS spectra (Fig. S11b–d†) reveal the presence of lattice oxygen (530.5 eV), adsorbed oxygen (533.2 eV), and surface hydroxyls (531.9 eV) in the samples.[58] Notably, the BEs of W 4f in WI10 display negative shifts in comparison with those in pure WO_3, while the peaks of In 3d in WI10 shift positively relative to pure In_2O_3. Such an intriguing phenomenon suggests the migration of electrons from In_2O_3 to WO_3 upon hybridization, creating an IEF with the direction from In_2O_3 to WO_3 at their interface to facilitate the efficient separation of photogenerated charge carriers (as discussed below).

3.3 Insights into the S-scheme charge separation mechanism

The band structure of WO_3 and In_2O_3 was first investigated to unravel the charge transfer and separation mechanism over WO_3/In_2O_3 heterojunctions. The potentials of the VB maximum and CB minimum of WO_3 and In_2O_3 are calculated to be 2.88 and 0.07 V, as well as 2.28 and −0.69 V (*vs.* RHE), respectively, based on Mott–Schottky plots, valence band XPS spectra (Fig. S13†) and the band gap (Fig. S10b†). According to the electrostatic potentials along the *z*-axis of WO_3 (001) and In_2O_3 (111) (Fig. S14†), the work function (Φ) of WO_3 and In_2O_3 is estimated to be 6.54 and 5.87 eV, respectively, indicating that In_2O_3 has a higher Fermi level (E_F) than WO_3. Additionally, the contact potential difference (CPD) between the samples and the standard gold tip of the Kelvin probe instrument reveals that the calculated Φ level of WO_3 is larger than that of In_2O_3 (Fig. S15†), aligning with the DFT results. As a consequence, electrons in In_2O_3 will spontaneously diffuse to WO_3 upon contact until reaching the same E_F at their interface, which will lead to the bending of their energy bands and the creation of an IEF pointing from In_2O_3 to WO_3 (Fig. 4c). The charge density difference of DFT simulation (Fig. 4d) shows that In_2O_3 donates electrons (cyan area) while WO_3 gains electrons (yellow area) at their interface, further confirming the above electron transfer pathway between WO_3 and In_2O_3.

Under light irradiation, the electrons in WO_3 and In_2O_3 VBs are initially photoexcited to their CBs. Due to the bent bands and IEF, the photogenerated electrons in the WO_3 CB tend to transfer to the In_2O_3 VB and recombine with its holes, indicating the formation of S-scheme heterojunctions between WO_3 and In_2O_3. Ultimately, the powerful photoelectrons in the In_2O_3 CB and photoholes in the WO_3 VB are reserved to participate in photocatalytic reactions (Fig. 4c). Such an S-scheme charge transfer route not only efficiently separates photoinduced

carriers, but also preserves the strong redox ability of surviving electrons and holes, thereby definitely enhancing CO_2 photoreduction performance and selectively producing CH_4.

In situ irradiation XPS was carried out to verify the proposed S-scheme charge transfer pathway within the WO_3/In_2O_3 heterostructure. As presented in Fig. 4a and b, the BEs of W 4f shift positively under illumination, while the In 3d BEs show negative shifts with reference to their respective values measured in the dark. These results support the transfer of photogenerated electrons from WO_3 to In_2O_3 and validate the suggested S-scheme photocatalytic mechanism. To gain a better understanding of how charge carriers are transferred in WO_3/In_2O_3 heterostructures, TRPL spectra of pure WO_3 and WI10 were collected under different atmospheres. As shown in Fig. 4e and Table S3,† the shorter lifetime (τ_1) of WI10 is only 0.76 ns in an Ar atmosphere, which is shorter than that of pure WO_3 (0.96 ns). This suggests that the photoexcited electrons in WO_3 transfer to In_2O_3 and the radiative recombination is retarded. Consequently, only a small fraction of photoelectrons of WI10 engage in the photocarrier recombination to emit fluorescence, resulting in shorter lifetimes of τ_2 and τ_3. These results provide further evidence for the S-scheme charge separation mechanism in WO_3/In_2O_3 heterojunctions. In addition, the average lifetime (τ_a) of WI10 in a CO_2 atmosphere is shorter compared to that in an Ar atmosphere (3.38 *vs.* 3.56 ns), which indicates that a great deal of photoinduced electrons in the In_2O_3 CB are delivered to CO_2 molecules for surface photoreduction and fewer photocarriers are involved in detectable recombination.[59,60] Photoelectrochemical measurements were further conducted to analyze the charge separation efficiency. As shown in Fig. S16,† WI10 displays higher photocurrent density and smaller charge transfer resistance (R_{ct}) as compared with pristine WO_3, indicating superior electron/hole separation efficiency and lower resistance for charge transfer in the WO_3/In_2O_3 S-scheme heterojunctions.[33,61]

Based on the aforementioned analyses, it is suggested that the combination of WO_3 and In_2O_3 to construct S-scheme heterojunctions can effectively promote charge transfer and reduce electron–hole recombination. In concert with the efficient adsorption and activation of CO_2 molecules on the In_2O_3 surface, the resulting WO_3/In_2O_3 S-scheme heterojunctions possess more photoelectrons with high reduction capacity to participate in the CO_2 photoreduction reaction and produce multi-electron products such as CH_4.

4. Conclusion

To summarize, an S-scheme WO_3/In_2O_3 heterojunction photocatalyst was constructed by depositing In_2O_3 nanoparticles on WO_3 nanosheets *via* a facile immersion-annealing method. DFT calculations, CO_2-TPD and *in situ* DRIFTS revealed that the WO_3/In_2O_3 heterostructures displayed efficient chemisorption and activation of CO_2 molecules. The difference in Fermi levels caused electrons to transfer from In_2O_3 to WO_3, thus forming an IEF and bending the energy bands at the interface, as evidenced by XPS and DFT results. Under light irradiation, photoinduced electrons in the WO_3 CB recombined with the holes in the In_2O_3

14866 | *J. Mater. Chem. A*, 2023, **11**, 14860–14869

This journal is © The Royal Society of Chemistry 2023

VB, driven by the bent bands and IEF, following an S-scheme charge transfer pathway and achieving efficient separation efficiency of powerful photogenerated charge carriers. As a result, the optimized WO_3/In_2O_3 heterojunctions exhibited enhanced CO_2 photoreduction performance with ~53.7% selectivity for CH_4, in the absence of any molecule cocatalyst or scavenger. The CO_2 photoreduction mechanism and underlying reasons for high CH_4-selectivity were uncovered *via in situ* DRIFTS, along with Gibbs free-energy calculations. This work offers a perspective on designing novel S-scheme heterojunction photocatalysts for efficient CO_2 photoreduction and selective conversion of CO_2 to CH_4.

Author contributions

Y. H., J. Y., and F. X. conceived and designed the experiments. Y. H. and Z. Y. conducted material synthesis, the characterizations of the materials, and the photocatalytic test. C. L. and Y. P. performed the SVUV-PIMS test. Y. H., J. Y., D. X., W. M., and F. X. contributed to data analysis. Y. H. wrote the manuscript. F. X. supervised the project, performed DFT calculations, and revised the manuscript. All authors discussed the results and commented on the manuscript.

Conflicts of interest

There are no conflicts to declare.

Acknowledgements

References

1 S. Patial, R. Kumar, P. Raizada, P. Singh, Q. Van Le, E. Lichtfouse, D. Le Tri Nguyen and V.-H. Nguyen, Boosting light-driven CO_2 reduction into solar fuels: Mainstream avenues for engineering ZnO-based photocatalysts, *Environ. Res.*, 2021, **197**, 111134.

2 J. Ma, X. Li, Y. Li, G. Jiao, H. Su, D. Xiao, S. Zhai and R. Sun, Single-atom zinc catalyst for co-production of hydrogen and fine chemicals in soluble biomass solution, *Adv. Powder Mater.*, 2022, **1**, 100058.

3 H. Zhao, R. Yu, S. Ma, K. Xu, Y. Chen, K. Jiang, Y. Fang, C. Zhu, X. Liu, Y. Tang, L. Wu, Y. Wu, Q. Jiang, P. He, Z. Liu and L. Tan, The role of Cu_1-O_3 species in single-atom Cu/ZrO_2 catalyst for CO_2 hydrogenation, *Nat. Catal.*, 2022, **5**, 818–831.

4 Y. Li, M. Zhang, L. Zhou, S. Yang, Z. Wu and Y. Ma, Recent Advances in Surface-Modified g-C_3N_4-Based Photocatalysts for H_2 Production and CO_2 Reduction, *Acta Phys.-Chim. Sin.*, 2021, **37**, 2009030.

5 W. Fu, J. Fan and Q. Xiang, Ag_2S Quantum Dots Decorated on Porous Cubic-CdS Nanosheets-assembled Flowers for Photocatalytic CO_2 Reduction, *Chin. J. Struct. Chem.*, 2022, **41**, 2206039–2206047.

6 X. Fei, H. Tan, B. Cheng, B. Zhu and L. Zhang, 2D/2D Black Phosphorus/g-C_3N_4 S-Scheme Heterojunction Photocatalysts for CO_2 Reduction Investigated using DFT Calculations, *Acta Phys.-Chim. Sin.*, 2021, **37**, 2010027.

7 V. Hasija, A. Kumar, A. Sudhaik, P. Raizada, P. Singh, Q. Van Le, T. T. Le and V.-H. Nguyen, Step-scheme heterojunction photocatalysts for solar energy, water splitting, CO_2 conversion, and bacterial inactivation: a review, *Environ. Chem. Lett.*, 2021, **19**, 2941–2966.

8 F. Xu, K. Meng, B. Cheng, S. Wang, J. Xu and J. Yu, Unique S-scheme heterojunctions in self-assembled $TiO_2/CsPbBr_3$ hybrids for CO_2 photoreduction, *Nat. Commun.*, 2020, **11**, 4613.

9 F. Xu, K. Meng, S. Cao, C. Jiang, T. Chen, J. Xu and J. Yu, Step-by-Step Mechanism Insights into the TiO_2/Ce_2S_3 S-Scheme Photocatalyst for Enhanced Aniline Production with Water as a Proton Source, *ACS Catal.*, 2022, **12**, 164–172.

10 B. Fang, Z. Xing, D. Sun, Z. Li and W. Zhou, Hollow semiconductor photocatalysts for solar energy conversion, *Adv. Powder Mater.*, 2022, **1**, 100021.

11 Z. Li, D. Wu, W. Gong, J. Li, S. Sang, H. Liu, R. Long and Y. Xiong, Highly Efficient Photocatalytic CO_2 Methanation over Ru-Doped TiO_2 with Tunable Oxygen Vacancies, *Chin. J. Struct. Chem.*, 2022, **41**, 2212043–2212050.

12 R. Das, S. Sarkar, R. Kumar, S. D. Ramarao, A. Cherevotan, M. Jasil, C. P. Vinod, A. K. Singh and S. C. Peter, Noble-Metal-Free Heterojunction Photocatalyst for Selective CO_2 Reduction to Methane upon Induced Strain Relaxation, *ACS Catal.*, 2022, **12**, 687–697.

13 X. An, Q. Tang, H. Lan, H. Liu, X. Yu, J. Qu, H. Lin and J. Ye, Facilitating Molecular Activation and Proton Feeding by Dual Active Sites on Polymeric Carbon Nitride for Efficient CO_2 Photoreduction, *Angew. Chem., Int. Ed.*, 2022, **61**, e2022127.

14 Z. Miao, Q. Wang, Y. Zhang, L. Meng and X. Wang, In situ construction of S-scheme AgBr/BiOBr heterojunction with surface oxygen vacancy for boosting photocatalytic CO_2 reduction with H_2O, *Appl. Catal., B*, 2022, **301**, 120802.

15 Y. Wang, H. Huang, Z. Zhang, C. Wang, Y. Yang, Q. Li and D. Xu, Lead-free perovskite $Cs_2AgBiBr_6$@g-C_3N_4 Z-scheme system for improving CH_4 production in photocatalytic CO_2 reduction, *Appl. Catal., B*, 2021, **282**, 119570.

16 M. Tahir and B. Tahir, Constructing S-scheme 2D/0D g-C_3N_4/TiO_2 NPs/MPs heterojunction with 2D-Ti_3AlC_2 MAX cocatalyst for photocatalytic CO_2 reduction to CO/CH_4 in fixed-bed and monolith photoreactors, *J. Mater. Sci. Technol.*, 2022, **106**, 195–210.

17 L. Wang, B. Zhu, J. Zhang, J. Ghasemi, M. Mousavi and J. Yu, S-scheme heterojunction photocatalysts for CO_2 reduction, *Matter*, 2022, **5**, 4187–4211.

18 X. Xiong, Y. Zhao, R. Shi, W. Yin, Y. Zhao, G. I. N. Waterhouse and T. Zhang, Selective photocatalytic CO_2 reduction over Zn-based layered double hydroxides

This journal is © The Royal Society of Chemistry 2023

J. Mater. Chem. A, 2023, **11**, 14860–14869 | **14867**

containing tri or tetravalent metals, *Sci. Bull.*, 2020, **65**, 987–994.

19 Z. Liu, S. Wu, M. Li and J. Zhang, Selective Photocatalytic CO_2 Reduction to CH_4 on Tri-s-triazine-Based Carbon Nitride via Defects and Crystal Regulation: Synergistic Effect of Thermodynamics and Kinetics, *ACS Appl. Mater. Interfaces*, 2022, **14**, 25417–25426.

20 S. Hu, Z. Deng, M. Xing, S. Wu and J. Zhang, Highly Dispersed Cobalt Centers on UiO-66-NH_2 for Photocatalytic CO_2 Reduction, *Catal. Lett.*, 2023, **153**, 1475–1482.

21 S. Hu, Z. Deng, M. Xing, S. Wu and J. Zhang, Construction of Cu cocatalyst on TiO_2 for regulating the selectivity of photocatalytic CO_2 reduction, *Res. Chem. Intermed.*, 2022, **48**, 3275–3287.

22 G. Han, C. Liu, Y. Pan, W. Macyk, S. Wageh, A. A. Al-Ghamdi and F. Xu, Artificial Photosynthesis over Tubular In_2O_3/ZnO Heterojunctions Assisted by Efficient CO_2 Activation and S-Scheme Charge Separation, *Adv. Sustain. Syst.*, 2023, **7**, 2200381.

23 H. Xu, Y. Wang, X. Dong, N. Zheng, H. Ma and X. Zhang, Fabrication of In_2O_3/In_2S_3 microsphere heterostructures for efficient and stable photocatalytic nitrogen fixation, *Appl. Catal., B*, 2019, **257**, 117932.

24 L. Wang and J. Yu, CO_2 capture and in situ photocatalytic reduction, *Chem Catal.*, 2022, **2**, 428–430.

25 L. Wang, C. Bie and J. Yu, Challenges of Z-scheme photocatalytic mechanisms, *Trends Chem.*, 2022, **4**, 973–983.

26 S. Wageh, A. A. Al-Ghamdi and L. Liu, S-Scheme Heterojunction Photocatalyst for CO_2 Photoreduction, *Acta Phys.-Chim. Sin.*, 2021, **37**, 2010024.

27 Z. Wang, B. Cheng, L. Zhang, J. Yu, Y. Li, S. Wageh and A. A. Al-Ghamdi, S-Scheme 2D/2D Bi_2MoO_6/BiOI van der Waals heterojunction for CO_2 photoreduction, *Chin. J. Catal.*, 2022, **43**, 1657–1666.

28 K. Alkanad, A. Hezam, Q. A. Drmosh, S. S. G. Chandrashekar, A. A. AlObaid, I. Warad, M. A. Bajiri and L. N. Krishnappagowda, Construction of Bi_2S_3/TiO_2/MoS_2 S-Scheme Heterostructure with a Switchable Charge Migration Pathway for Selective CO_2 Reduction, *Sol. RRL*, 2021, **5**, 2100501.

29 L. Zhang, J. Zhang, H. Yu and J. Yu, Emerging S-Scheme Photocatalyst, *Adv. Mater.*, 2022, **34**, 2107668.

30 F. A. Qaraah, S. A. Mahyoub, A. Hezam, A. Qaraah, F. Xin and G. Xiu, Synergistic effect of hierarchical structure and S-scheme heterojunction over O-doped g-C_3N_4/N-doped Nb_2O_5 for highly efficient photocatalytic CO_2 reduction, *Appl. Catal., B*, 2022, **315**, 121585.

31 Q. Xu, L. Zhang, B. Cheng, J. Fan and J. Yu, S-Scheme Heterojunction Photocatalyst, *Chem*, 2020, **6**, 1543–1559.

32 Z. Wang, B. Cheng, L. Zhang, J. Yu and H. Tan, BiOBr/NiO S-Scheme Heterojunction Photocatalyst for CO_2 Photoreduction, *Sol. RRL*, 2022, **6**, 2100587.

33 Y. Lin, G. Huang, L. Chen, J. Zhang and L. Liu, Enhanced CO_2 Photoreduction by $Ni(OH)_{2-x}$/WO_3 Nanofibers with Efficient CO_2 Activation and Charge Separation, *Adv. Sustain. Syst.*, 2022, **7**, 2200364.

34 W. Shi, X. Guo, C. Cui, K. Jiang, Z. Li, L. Qu and J. Wang, Controllable synthesis of Cu_2O decorated WO_3 nanosheets with dominant (001) facets for photocatalytic CO_2 reduction under visible-light irradiation, *Appl. Catal., B*, 2019, **243**, 236–242.

35 Y. Yang, Y. Pan, X. Tu and C. Liu, Nitrogen doping of indium oxide for enhanced photocatalytic reduction of CO_2 to methanol, *Nano Energy*, 2022, **101**, 107613.

36 S. Wang, B. Guan and X. Lou, Construction of $ZnIn_2S_4$-In_2O_3 Hierarchical Tubular Heterostructures for Efficient CO_2 Photoreduction, *J. Am. Chem. Soc.*, 2018, **140**, 5037–5040.

37 Z. Deng, S. Hu, J. Ji, S. Wu, H. Xie, M. Xing and J. Zhang, Deep insight of the influence of Cu valence states in co-catalyst on CO_2 photoreduction, *Appl. Catal., B*, 2022, **316**, 121621.

38 J. Li, X. Pei, Z. Wang, Y. Li and G. Zhang, Boosted charge transfer and selective photocatalytic CO_2 reduction to CH_4 over sulfur-doped $K_{0.475}WO_3$ nanorods under visible light: Performance and mechanism insight, *Appl. Surf. Sci.*, 2022, **605**, 154632.

39 M. Li, Z. Liu, S. Wu and J. Zhang, Advances for CO_2 Photocatalytic Reduction in Porous Ti-Based Photocatalysts, *ACS ES&T Eng.*, 2022, **2**, 942–956.

40 S. Hu, C. Dong, Z. Deng, M. Xing and J. Zhang, Tuning Reaction Pathway of CO_2 Photoreduction via PtRu Bimetallic Microstructure Regulation, *J. Phys. Chem. C*, 2021, **125**, 10406–10412.

41 Y. Pu, Y. Luo, X. Wei, J. Sun, L. Li, W. Zou and L. Dong, Synergistic effects of Cu_2O-decorated CeO_2 on photocatalytic CO_2 reduction: Surface Lewis acid/base and oxygen defect, *Appl. Catal., B*, 2019, **254**, 580–586.

42 J. Zhao, Y. Wang, Y. Li, X. Yue and C. Wang, Phase-dependent enhancement for CO_2 photocatalytic reduction over CeO_2/TiO_2 catalysts, *Catal. Sci. Technol.*, 2016, **6**, 7967–7975.

43 A. Meng, B. Cheng, H. Tan, J. Fan, C. Su and J. Yu, TiO_2/polydopamine S-scheme heterojunction photocatalyst with enhanced CO_2-reduction selectivity, *Appl. Catal., B*, 2021, **289**, 120039.

44 S. Wageh, O. A. Al-Hartomy, M. F. Alotaibi and L. Liu, Ionized cocatalyst to promote CO_2 photoreduction activity over core-triple-shell ZnO hollow spheres, *Rare Met.*, 2022, **41**, 1077–1079.

45 M. Sayed, F. Xu, P. Kuang, J. Low, S. Wang, L. Zhang and J. Yu, Sustained CO_2-photoreduction activity and high selectivity over Mn, C-codoped ZnO core-triple shell hollow spheres, *Nat. Commun.*, 2021, **12**, 4936.

46 X. Li, Y. Sun, J. Xu, Y. Shao, J. Wu, X. Xu, Y. Pan, H. Ju, J. Zhu and Y. Xie, Selective visible-light-driven photocatalytic CO_2 reduction to CH_4 mediated by atomically thin $CuIn_5S_8$ layers, *Nat. Energy*, 2019, **4**, 690–699.

47 K. Wang, J. Lu, Y. Lu, C. Lau, Y. Zheng and X. Fan, Unravelling the C-C coupling in CO_2 photocatalytic reduction with H_2O on Au/TiO_2-x: Combination of plasmonic excitation and oxygen vacancy, *Appl. Catal., B*, 2021, **292**, 120147.

14868 | *J. Mater. Chem. A*, 2023, **11**, 14860–14869

This journal is © The Royal Society of Chemistry 2023

48 Y. Zeng, Z. Tang, X. Wu, A. Huang, X. Luo, G. Q. Xu, Y. Zhu and S. L. Wang, Photocatalytic oxidation of methane to methanol by tungsten trioxide-supported atomic gold at room temperature, *Appl. Catal., B*, 2022, **306**, 120919.

49 L. Liu, H. Zhao, J. M. Andino and Y. Li, Photocatalytic CO_2 Reduction with H_2O on TiO_2 Nanocrystals: Comparison of Anatase, Rutile, and Brookite Polymorphs and Exploration of Surface Chemistry, *ACS Catal.*, 2012, **2**, 1817–1828.

50 J. Sheng, Y. He, J. Li, C. Yuan, H. Huang, S. Wang, Y. Sun, Z. Wang and F. Dong, Identification of Halogen-Associated Active Sites on Bismuth-Based Perovskite Quantum Dots for Efficient and Selective CO_2-to-CO Photoreduction, *ACS Nano*, 2020, **14**, 13103–13114.

51 Y. Liu, D. Shen, Q. Zhang, Y. Lin and F. Peng, Enhanced photocatalytic CO_2 reduction in H_2O vapor by atomically thin Bi_2WO_6 nanosheets with hydrophobic and nonpolar surface, *Appl. Catal., B*, 2021, **283**, 119630.

52 X. Yang, S. Wang, N. Yang, W. Zhou, P. Wang, K. Jiang, S. Li, H. Song, X. Ding, H. Chen and J. H. Ye, Oxygen vacancies induced special CO_2 adsorption modes on Bi_2MoO_6 for highly selective conversion to CH_4, *Appl. Catal., B*, 2019, **259**, 118088.

53 H. Yu, M. Wang, J. Yan, H. Dang, H. Zhu, Y. Liu, M. Wen, G. Li and L. Wu, Complete mineralization of phenolic compounds in visible-light-driven photocatalytic ozonation with single-crystal WO_3 nanosheets: Performance and mechanism investigation, *J. Hazard. Mater.*, 2022, **433**, 128811.

54 S. Cao, J. Yu, S. Wageh, A. A. Al-Ghamdi, M. Mousavi, J. B. Ghasemi and F. Xu, H_2-production and electron-transfer mechanism of a noble-metal-free $WO_3@ZnIn_2S_4$ S-scheme heterojunction photocatalys, *J. Mater. Chem. A*, 2022, **10**, 17174–17184.

55 S. Li, M. Cai, Y. Liu, C. Wang, R. Yan and X. Chen, Constructing $Cd_{0.5}Zn_{0.5}S/Bi_2WO_6$ S-scheme heterojunction for boosted photocatalytic antibiotic oxidation and Cr(VI) reduction, *Adv. Powder Mater.*, 2023, **2**, 100073.

56 S. Han, B. Li, L. Huang, H. Xi, Z. Ding and J. Long, Construction of $ZnIn_2S_4$-$CdIn_2S_4$ Microspheres for Efficient Photo-catalytic Reduction of CO_2 with Visible Light, *Chin. J. Struct. Chem.*, 2022, **41**, 2201007–2201013.

57 L. Yin, D. Chen, M. Hu, H. Shi, D. Yang, B. Fan, G. Shao, R. Zhang and G. Shao, Microwave-assisted growth of In_2O_3 nanoparticles on WO_3 nanoplates to improve H_2S-sensing performance, *J. Mater. Chem. A*, 2014, **2**, 18867–18874.

58 B. Lei, W. Cui, P. Chen, L. Chen, J. Li and F. Dong, C-Doping Induced Oxygen-Vacancy in WO_3 Nanosheets for CO_2 Activation and Photoreduction, *ACS Catal.*, 2022, **12**, 9670–9678.

59 S. Nayak, L. Mohapatra and K. Parida, Visible light-driven novel g-C_3N_4/NiFe-LDH composite photocatalyst with enhanced photocatalytic activity towards water oxidation and reduction reaction, *J. Mater. Chem. A*, 2015, **3**, 18622–18635.

60 Y. Hu, X. Hao, Z. Cui, J. Zhou, S. Chu, Y. Wang and Z. Zou, Enhanced photocarrier separation in conjugated polymer engineered CdS for direct Z-scheme photocatalytic hydrogen evolution, *Appl. Catal., B*, 2020, **260**, 118131.

61 M. Sayed, B. Zhu, P. Kuang, X. Liu, B. Cheng, A. A. Al Ghamdi, S. Wageh, L. Zhang and J. Yu, EPR Investigation on Electron Transfer of 2D/3D g-C_3N_4/ZnO S-Scheme Heterojunction for Enhanced CO_2 Photoreduction, *Adv. Sustain. Syst.*, 2022, **6**, 2100264.

This journal is © The Royal Society of Chemistry 2023

J. Mater. Chem. A, 2023, **11**, 14860–14869 | **14869**